



# An Efficient and Robust Surface-Modified Iron Electrode for Oxygen Evolution in Alkaline Water Electrolysis

D. Mitra,<sup>1,\*</sup> P. Trinh,<sup>1</sup> S. Malkhandi,<sup>1</sup> M. Mecklenburg,<sup>2</sup> S. M. Heald,<sup>3</sup>  
M. Balasubramanian,<sup>1b</sup> and S. R. Narayanan<sup>1b,\*\*,z</sup>

<sup>1</sup>Loker Hydrocarbon Research Institute, University of Southern California, Los Angeles, California 90089, USA

<sup>2</sup>Center for Electron Microscopy and Microanalysis, University of Southern California, Los Angeles, California 90089-0101, USA

<sup>3</sup>Advanced Photon Source, Argonne National Laboratory, Lemont, Illinois 60439, USA

Iron is unstable as an oxygen evolution electrode in alkaline media. Thus, relatively expensive nickel-based electrodes are used in industrial alkaline water electrolysis. We show that an iron substrate can be rendered stable and electrocatalytically active for the oxygen evolution reaction by nano-scale surface modification with nickel. The electrocatalytic activity of such a surface-modified iron electrode is comparable to the recently-reported nickel-based catalysts. The electrocatalytic activity is due to a 50-nanometer layer of a high-surface area  $\alpha$ -nickel hydroxide on the iron electrode. The nickel modification renders the iron electrode electrically-conductive, prevents dielectric breakdown, and thus endows anodic stability. The electrocatalytic activity is unchanged even after 1000 hours of continuous operation. The temperature of preparation is critical, as excessive dehydration of the hydroxide layer results in nickel ferrite formation and a drastic reduction in electrocatalytic activity. We report significant insight into the surface chemical composition and structure of the catalyst layer by X-ray Absorption Spectroscopy, Photoelectron Spectroscopy, and Transmission Electron Microscopy. Electrochemical kinetics analysis suggests that surface hydroxo-intermediates react with the hydroxide ions from the solution to evolve oxygen. Thus, the surface-modified iron substrates present an opportunity for improving the performance and reducing the cost of alkaline water electrolysis systems.

© The Author(s) 2018. Published by ECS. This is an open access article distributed under the terms of the Creative Commons Attribution 4.0 License (CC BY, <http://creativecommons.org/licenses/by/4.0/>), which permits unrestricted reuse of the work in any medium, provided the original work is properly cited. [DOI: 10.1149/2.1371805jes]



Manuscript submitted January 15, 2018; revised manuscript received April 4, 2018. Published April 14, 2018. This was Paper 53 presented at the Honolulu, Hawaii, Meeting of the Society, October 2–7, 2016.

Inexpensive, efficient and durable electrocatalysts for supporting oxygen evolution are direly needed for reducing the cost and improving the performance of water electrolysis systems and metal-air batteries. The sluggish kinetics of the multi-electron charge-transfer during oxygen evolution results in large overpotentials and reduced energy efficiency.<sup>1–14</sup> Although ruthenium and iridium-based electrocatalysts are very active for the oxygen evolution reaction (OER), these electrocatalysts are simply not stable in alkaline media.<sup>15–19</sup> Further, the cost of these noble metals is prohibitive for large-scale utilization of such electrocatalysts.<sup>16,20</sup> Consequently, electrodes based on transition metal oxides supported on nickel substrates are the preferred catalysts for industrial alkaline water electrolysis.<sup>21</sup> Recent studies have indicated exciting possibilities with a variety of alternative catalyst materials that do not use noble metals.<sup>22–27</sup> Specifically, transition metal perovskite and spinel oxides, and layered-double-hydroxides containing iron, nickel, and cobalt are promising.<sup>25–35</sup> Also, nitrogen and phosphorous-doped carbon-based catalysts have shown significant electrocatalytic activity.<sup>36</sup> The relatively harsh conditions imposed by the anodic potentials during oxygen evolution present a major challenge to the chemical stability of these electrocatalysts. Thus, despite the progress, an inexpensive electrocatalyst that is simultaneously efficient and robust for the large-scale utilization continues to be a challenge. The findings that we report here suggest a new opportunity for advancing the field of alkaline water electrolysis.

The inherent stability of nickel under anodic conditions has led to its wide use as a substrate for oxygen electrodes in alkaline media. Also, recent discoveries emphasize the enhanced catalytic activity achieved by the addition of small amounts of iron to nickel oxide and hydroxides.<sup>37–41</sup> For water electrolysis systems, the cost added by nickel-based electrodes for the anode and cathode can be quite significant, and its replacement by less expensive materials is much desired. Further, improvements in energy efficiency are desired to lower the cost of hydrogen production.

Iron is at least 40 times less expensive than nickel. Thus, we were urged to consider iron as an alternate electrode material. However,

an iron electrode when anodically polarized in alkali at the potentials of the oxygen evolution reaction produces copiously oxidized forms of iron, and the electrode disintegrates rapidly. Specifically, a passive protective film of iron (III) oxide is first formed on the surface of iron, and then this film being insulating breaks down under anodic conditions resulting in further exposure of bare iron to the alkaline electrolyte. For this reason, it has been so far impractical to use iron as a substrate or electrode for evolving oxygen (see supplementary information, Fig. S1). Attempts to improve the durability of the iron electrode with magnetite coatings has met with limited success in other anode applications.<sup>42</sup> Thus, iron remains unutilized as an electrode material for oxygen evolution in alkaline media.

We report a surface-modified iron electrode that is remarkably stable and exhibits significant electrocatalytically activity for the oxygen evolution reaction. Specifically, we show that a porous sintered iron structure fabricated from carbonyl iron powder can be modified to be an efficient and robust electrode for alkaline water electrolysis. The electrochemical performance of such a surface-modified iron electrode for oxygen evolution is comparable to the recent nickel and cobalt-based iron hydroxide electrodes.<sup>27,43</sup> The present study, focuses on gaining insight into the mechanism of electrocatalytic activity, understanding the effect of preparation conditions, and investigating the durability of the electrocatalyst under extended operation for 1000 hours.

## Experimental

**Preparation of surface-modified iron electrodes.**—All surface-modified iron electrodes were prepared using a three-step process:

- Step 1. Sintering of carbonyl iron powder to form a porous iron substrate,
- Step 2. Application of a precursor coating at 100–150°C, and
- Step 3. Heating of the precursor coating in air at 200°C or 400°C to induce modification of the iron surface.

The iron substrate was prepared by sintering a 1:1 mixture of carbonyl iron powder (BASF SM grade) and ammonium bicarbonate (ReagentPlus,  $\geq 99.0\%$ ) in a tube furnace under argon atmosphere at 850°C for 15 minutes. Upon heating, the ammonium bicarbonate

\*Electrochemical Society Student Member.

\*\*Electrochemical Society Fellow.

<sup>z</sup>E-mail: [srnaraya@usc.edu](mailto:srnaraya@usc.edu)

decomposed to ammonia, water and carbon dioxide leaving behind pores within the sintered structure. The electrodes were typically 5 cm × 4 cm in size with a thickness of about 0.5 mm.

In Step 2, the iron substrate was heated to about 150°C and an aqueous solution of nickel nitrate was spread dropwise on the hot surface to form an evaporated layer. We term this layer as the “precursor” coating. Such a precursor-coated electrode was heated in air at 200°C or 400°C for 30 minutes (at a heating rate of 10°C per minute) during which the precursor decomposed on the surface of the iron electrode.

Steps 2 and 3 were repeated to achieve the targeted mass increase of 7.5 mg cm<sup>-2</sup>. The electrodes prepared by heat-treatment at 200°C and 400°C have been designated as NSI-200 and NSI-400, respectively.

#### Physical characterization- morphology and phase studies.—

Scanning electron microscopy (SEM) (conducted with JSM-7001F) was used to study the surface morphology of the electrodes “as-prepared” and after electrochemical tests. Electrodes that were subjected to electrochemical stability tests were thoroughly washed in de-ionized water and dried in air prior to SEM analysis.

Surface morphology, thickness of the oxide coating, and elemental distribution across the coating was probed by transmission electron microscopy (TEM). Sub-100 nm thick cross-sections of the samples were prepared using standard focused ion beam-sample preparation-techniques (FEI Nova 600 NanoLab DualBeam) and the resulting lamella was imaged using a TEM (JEOL JEM-2100F) at an accelerating voltage of 200kV.

To obtain the degree of crystallinity and the phase composition all the samples were investigated by X-ray diffraction using a Rigaku Ultima IV diffractometer (Cu K-alpha source). X-ray photoelectron spectroscopy (Kratos Axis Ultra DLD) was used to investigate the surface oxidation states of the components in the samples. Samples for both X-ray diffraction (XRD) and X-ray photoelectron spectroscopy (XPS) studies were handled in just the same manner as that for the SEM studies.

Nickel K-edge X-ray Absorption Fine Structure (XAFS) measurements were made on beamline 20-ID-C at the Advanced Photon Source (Argonne National Laboratory). The first harmonic of the undulator was used along with full scanning of the undulator. The incident beam was rendered monochromatic using a Si (111) double crystal monochromator. The X-ray beam was focused using a toroidal mirror and the beam was defined [0.1 mm (vertical) by 0.4 mm (horizontal)] using a pair of slits. Higher-order harmonics were suppressed by de-tuning the monochromator to reduce the incident X-ray intensity by approximately 15%. A bent Laue analyzer (FMB Oxford) in conjunction with a 2D-position sensitive detector (Pilatus 100K) was employed to reject the large and detrimental Fe fluorescence background and to selectively monitor the dilute Ni K<sub>α</sub> fluorescence from the modified electrodes. For comparison, transmission-mode XAFS data of α-Ni(OH)<sub>2</sub> were obtained in beamline 20-BM-B. Data reduction was carried out using the IFEFFIT suite of software.<sup>44</sup>

**Polarization measurements.**—We measured the electrocatalytic activity for the oxygen evolution reaction by steady-state potentiostatic polarization experiments. These measurements were made by holding at each value of potential for 15 minutes. Linear sweep voltammetry was specifically avoided to ensure that any slow changes to the surface chemistry did not interfere with the accurate determination of the kinetic parameters. Both the oxygen evolution activity and reaction-order studies were performed at room temperature close to 25°C. However, for measuring the activation energy the temperature was varied between 30°C and 50°C at intervals of 5°C.

For all the electrochemical measurements we used a three-electrode polyfluoroethylene cell with a mercury/mercuric oxide (MMO) reference electrode (in a 5.35 M potassium hydroxide aqueous solution), a nickel mesh as counter electrode and 5.35 M potassium hydroxide aqueous solution as the electrolyte. We have selected this concentration of electrolyte for testing because it is widely used in commercial water electrolysis. We recognize that some of the data in the recent literature is with 1 M potassium hydroxide. To allow

comparisons with the literature data, we have reported all potentials vs. the reversible hydrogen electrode. Thus, electrode potentials measured against MMO were recalculated vs. the Reversible Hydrogen Electrode (RHE) scale using the relationship,

$$E_{\text{RHE}} = E_{\text{MMO}} + 0.098 \text{ V} + 0.828 \text{ V} + 0.059 \log a_{\text{OH}^-}, \text{ at } 25^\circ\text{C}$$

where  $E_{\text{RHE}}$  in the equation refers to the potential of the electrode vs. RHE,  $E_{\text{MMO}}$  is the potential vs. MMO and  $a_{\text{OH}^-}$  is the activity of hydroxide ions in the electrolyte.<sup>45</sup>

By using the same concentration of potassium hydroxide solution in the MMO electrode as in the electrolyte we avoided liquid junction potentials. However, for determining the reaction order with respect to OH<sup>-</sup> ions, we varied the concentration of potassium hydroxide aqueous solution in the cell set up and corrected for the liquid junction potential. High-purity water (18.2 MOhm-cm, 4 ppb total organic carbon) was used to prepare the electrolyte solutions. Since the measured currents were as high as 2 Amperes in some of the cases, the measured electrode potential values were corrected for the potential drop due to the uncompensated solution resistance between the working and reference electrodes.

**Electrochemical impedance spectroscopy (EIS).**—Electrochemical impedance at various values of electrode potential was measured in the frequency range of 10 kHz to 1 Hz with a sinusoidal voltage excitation (2 mV peak to peak). We measured the double-layer capacitance in the potential range where oxygen evolution occurred. Double-layer capacitance was determined by fitting the complex impedance data to a modified Randles-type equivalent circuit that included the constant phase element to represent the distributed capacitance arising from the high-surface area of the electrode. We calculated the double-layer capacitance from the parameters of the constant phase element using the relationship in Eq. 1.

$$C_{\text{DL}} = [Q_0(1/R_s + 1/R_{\text{ct}})^{a-1}]^{1/a} \quad [1]$$

where,  $C_{\text{DL}}$  is the double-layer capacitance in farad (F),  $Q_0$  is the constant phase element with the unit S-sec<sup>a</sup>, “a” is the unit-less exponent (0 < a < 1).  $R_s$  and  $R_{\text{ct}}$  refer to solution resistance and charge-transfer resistance, respectively.<sup>46</sup>

## Results and Discussion

**Electrode structure and phase composition.**—The iron electrode (Fig. 1) prepared by the sintering of carbonyl iron particles had a macro-porous structure consisting of a framework of iron particles connected by sinter “necks” that formed open pores suited for electrolyte access much like the nickel foam electrodes used in industrial water electrolysis (Fig. 1). The porosity of the iron electrodes was determined to be 80.6% v/v. The size of the pores in the iron electrodes ranged from 5 to 500 microns.

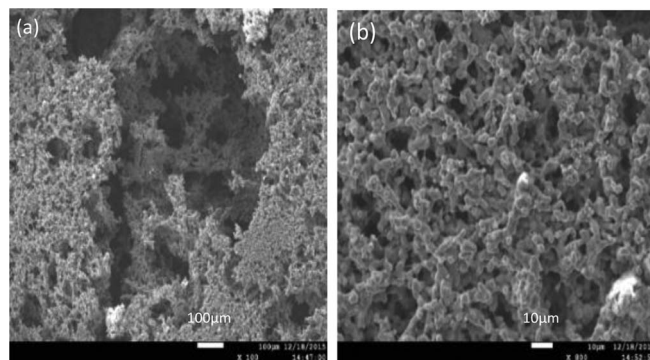


**Figure 1.** SEM images of iron substrate: (a) microporous structure and, (b) sintered necks formed by iron particles.

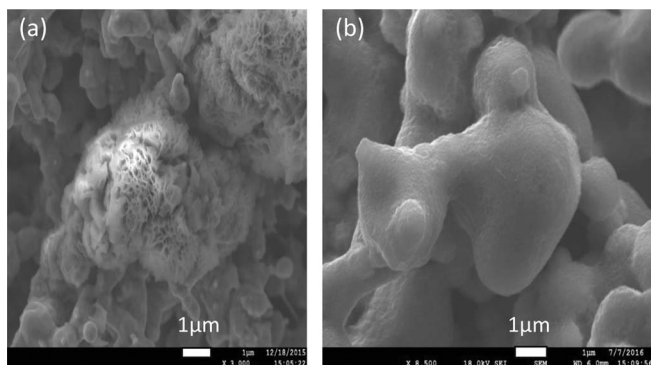


**Figure 2.** SEM images: (a) as-prepared NSI-200 showing flake like nano-structure and, (b) NSI-400.

After surface modification, the NSI-200 electrodes (designation of those electrodes prepared at 200°C) showed a flake-like heterogeneous nano-structure. However, the NSI-400 electrodes (designation of the electrodes prepared at 400°C) appeared to be smooth compared to the NSI-200 electrodes (Fig. 2).

The electrochemical impedance measurements yielded a complex impedance plot with a slightly depressed semi-circle indicative of the distributed nature of the capacitance and resistance elements at the interface typical of a microporous surface (Fig. 3). The impedance data was fitted to a modified Randles' equivalent circuit (see supplementary information, Table S1 for values of fit parameters). We confirmed that the choice of this equivalent circuit was physically meaningful based on the observed decrease of charge-transfer resistance parameter with increasing applied potential. The double layer capacitance was calculated from the constant-phase element parameter using the relationship in Eq. 1. We found that the double-layer capacitance of the NSI-200 electrodes was at least 140 times that of the NSI-400 electrodes (Table I). The area enhancement is consistent with the significant differences in morphology observed for NSI-200 and NSI-400 (Fig. 2). The charge-transfer resistance of NSI-200 was approximate 100 times lower than that of NSI-400.

The NSI-200 electrodes showed an amorphous surface while the NSI-400 electrodes showed nano-crystallinity (Fig. 4). We attribute the amorphous nature of the sample prepared at 200°C to a surface of iron and nickel hydroxides. We expect such hydroxides to be stable to about 250°C. When the preparation temperature was raised to 400°C, the iron and nickel hydroxide were expected to dehydrate, consistent with the formation of a crystalline oxide phase. While we do not

**Table I. Double-layer capacitance and charge-transfer resistance normalized for geometric area of electrode for NSI-200 and NSI-400 at 1.53 V vs RHE.**

Sample	Double-Layer Capacitance, $C_{DL}$ , $F\ cm^{-2}$	Charge-transfer resistance, $R_{ct}$ , $\Omega\text{-cm}^2$
NSI-200	$3.89 \times 10^{-4}$	0.42
NSI-400	$2.74 \times 10^{-6}$	4.18

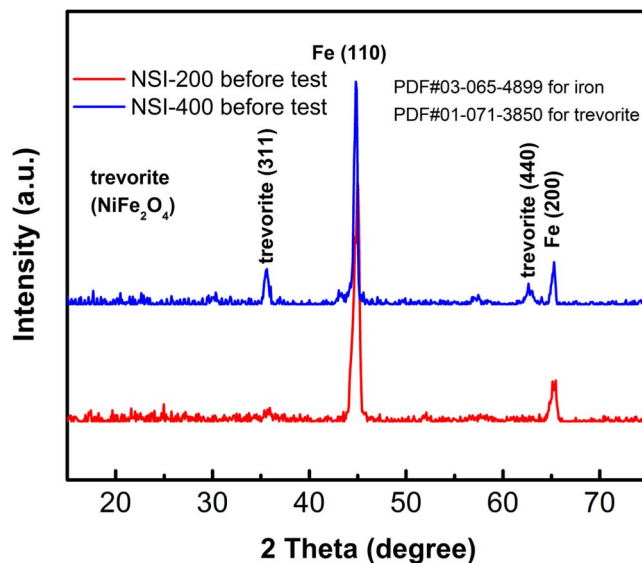


**Figure 4.** X-ray diffraction pattern of NSI-200 and NSI-400 in the “as-prepared” state before electrochemical testing.

expect complete transformation to a crystalline oxide until 500°C, we noticed the beginnings of the formation of trevorite (nickel ferrite spinel,  $NiFe_2O_4$ ) in the NSI-400.<sup>47</sup> Using the Scherrer formula and the full-width at half maximum for the (311) peaks, we calculated the crystallite size for the trevorite phase in NSI-400 sample to be 34 nm.

The XAFS and XPS investigations provided further insight into the above findings. The XAFS  $\chi(k)$  of NSI-200 was similar to that of the  $\alpha$ - $Ni(OH)_2$ , while that of NSI-400 was distinctly different (See Fig. S2 in Supplementary information). This finding was also borne out in the corresponding Fourier transforms (FTs) shown in Figs. 5a, 5b. The first feature in the FT (ca. 1–2 Å) is ascribed to Ni-O correlations in

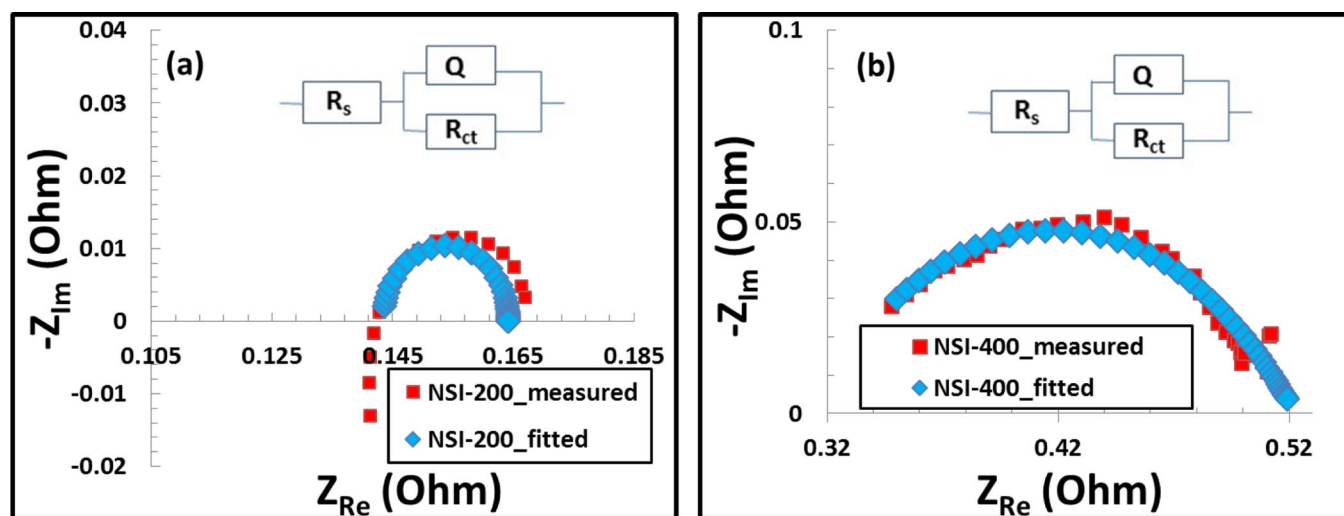


**Figure 3.** Measured and fitted EIS data: (a) NSI-200 and (b) NSI-400. Fitting was done using the modified Randles' circuit shown in the inset.

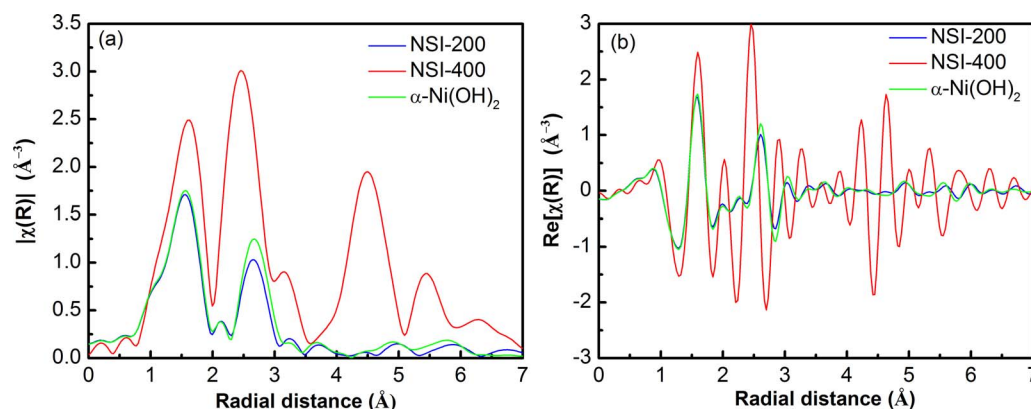


**Figure 5.** (a) The magnitude of FT and (b) the real part of FT corresponding to NSI-200, NSI-400 and  $\alpha\text{-Ni(OH)}_2$ .

all cases. Both NSI-200 and  $\alpha\text{-Ni(OH)}_2$  samples showed a relatively strong second feature (ca. 2.2–3  $\text{\AA}$ ). This feature corresponded to Ni-Ni correlations that arose from edge-shared  $\text{NiO}_6$  octahedral units.<sup>48,49</sup> As such, the general appearance of the FT of NSI-200 was similar to  $\alpha\text{-Ni(OH)}_2$ , even out to 6  $\text{\AA}$ . These observations revealed that the nickel in NSI-200 was present as a hydrated, non-crystalline  $\alpha\text{-Ni(OH)}_2$ .

In contrast, the FT of NSI-400 was very different from  $\alpha\text{-Ni(OH)}_2$ . The FT features of NSI-400 were of higher intensity, which suggested a more ordered structure. The features in the region 2–3.5  $\text{\AA}$  was ascribed to Ni-metal correlations from dominant octahedral-octahedral and additional octahedral-tetrahedral-correlations. Indeed, the spectrum was consistent with nickel largely occupying octahedral sites in a spinel structure.<sup>50,51</sup> The presence of an octahedral-tetrahedral correlation pointed to tetrahedral site occupancy (likely  $\text{Fe}^{3+}$ ), which was expected for a nickel ferrite (an inverse spinel). Therefore, these findings were consistent with XRD analysis and revealed the presence of distinctly different nickel modified surface phases in NSI-200 and NSI-400 samples.

TEM studies indicated that both the NSI-200 and NSI-400 samples have a core consisting of iron surrounded by two recognizable over-layers (Fig. 6). The layer immediately surrounding the iron core was an iron oxide phase whereas the outer-most layer, in the case of NSI-200 is comparatively nickel-rich ( $\text{Ni}:\text{O} = 36:65$ ), which was consistent with the XAFS finding of alpha-nickel hydroxide. Thickness of this outer-most layer was between 50 to 80 nm in case of NSI-200 (Fig. S3). For NSI-400 sample, the outer layer was had a lower nickel content than NSI-200, with  $\text{Ni}:\text{O} = 8:92$ , which was also consistent with the XAFS results of a spinel ferrite (trevorite) phase ( $\text{NiFe}_2\text{O}_4$ ). The thickness of this nickel ferrite phase was about 60–90 nm (Fig. S3).

**Surface composition.**—XPS investigations of the electrode surfaces in the as-prepared state (i.e., before any wet electrochemical

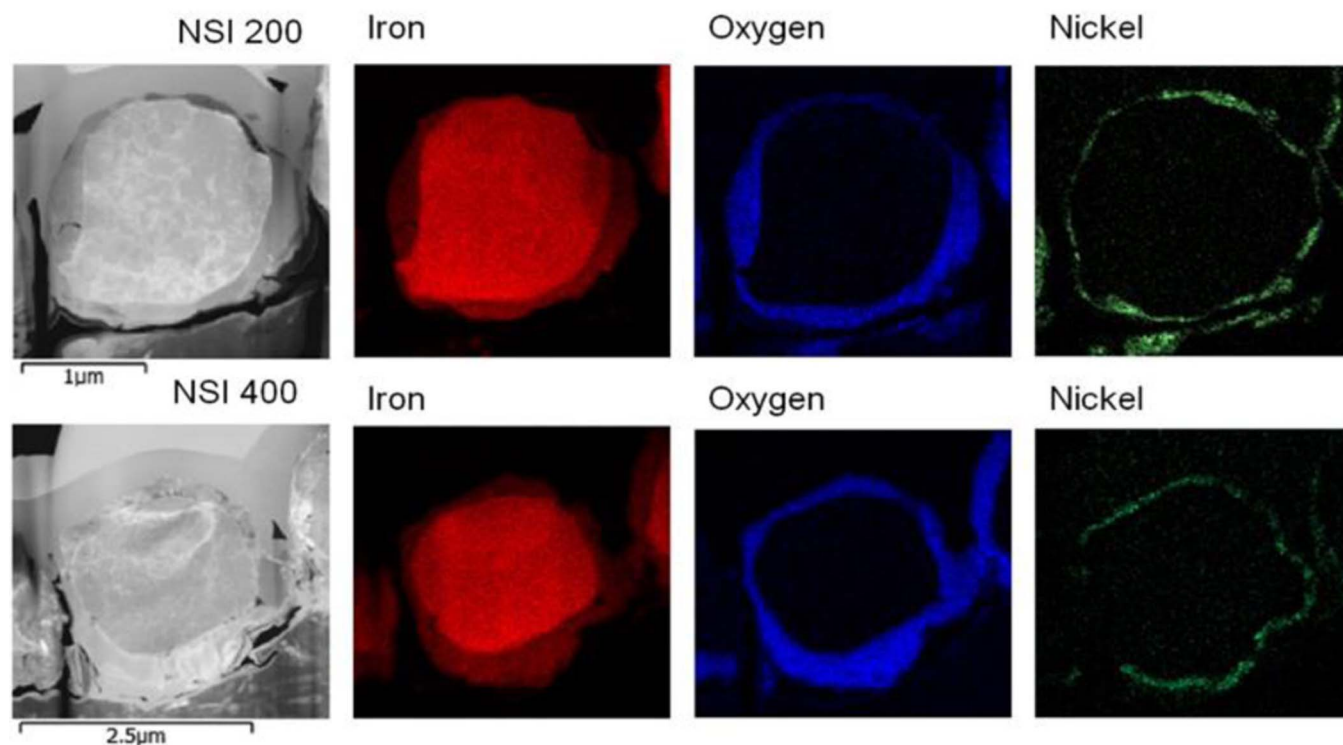


**Figure 6.** TEM analysis of NSI-200 and NSI-400.

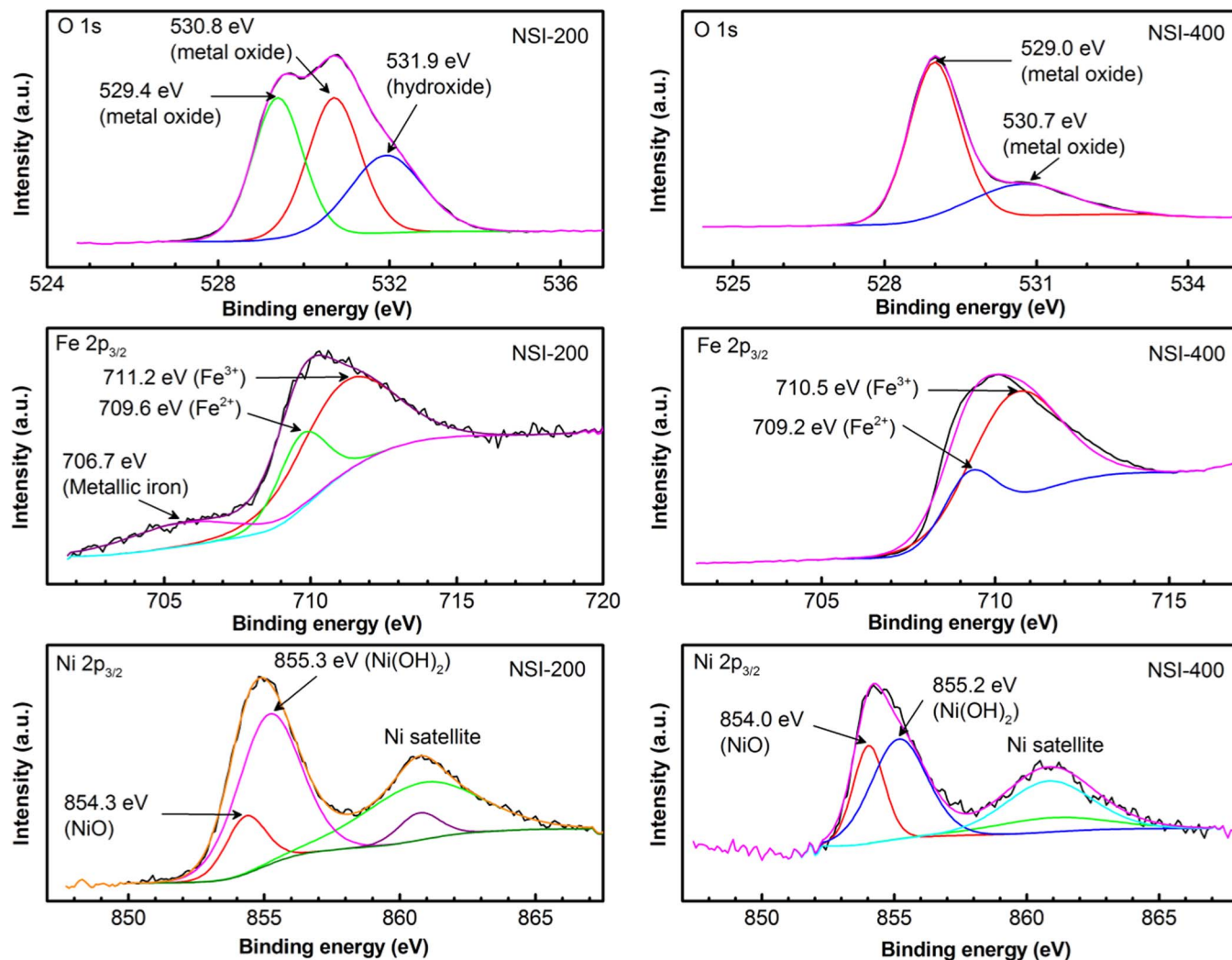


**Figure 7.** Binding energy of oxygen (1s), iron (2p) and nickel (2p) for NSI-200 and NSI-400 in the as prepared state.

testing) indicated that nickel and iron were in the oxidized state and support the findings from XAFS and XRD studies (Fig. 7). We have made assignments of the XPS data based on previously reported values for the respective oxides and hydroxides of nickel and iron in different materials.<sup>52–54</sup> For the NSI-200 sample, we noted a small fraction of iron still in the metallic state.

The oxygen 1s peaks were de-convoluted based on oxides (529.4 eV and 530.7 eV)<sup>50</sup> and hydroxides (531.9 eV)<sup>53</sup> for both NSI-200 and NSI-400, with only oxides being observed with NSI-400. The dominant presence of oxides on the NSI-400 electrode is consistent with the dehydration at the higher temperature of preparation and the formation of the trevorite phase seen by XRD. The binding energy values for the iron-2p<sub>3/2</sub> ranged from 706.5 eV to 712.5 eV. These asymmetric peaks were de-convoluted to indicate the presence of Fe<sup>3+</sup>, Fe<sup>2+</sup> and metallic iron on the surface of NSI-200. The area under the de-convoluted peaks had a distribution ratio for Fe<sup>3+</sup> to Fe<sup>2+</sup> of 2.5:1 for NSI-200 and 3:1 for NSI-400. The higher average oxidation state of iron in the NSI-400 is consistent with the Fe<sup>3+</sup> in NiFe<sub>2</sub>O<sub>4</sub> as indicated by the XRD study (Fig. 4). For the NSI-200 sample, we noted that a small fraction of iron was still in the metallic state suggesting that some areas of the electrode may be covered by a very thin layer of oxide/hydroxide allowing the X-rays to probe below the surface.

After the surface modification, the iron electrodes were extremely stable during anodic polarization in alkali solutions for at least 1000 hours (see later here for data). Such stability of the surface-modified

iron electrode was in sharp contrast to the rapid disintegration and discoloration of the solution (turning brown) when the unmodified iron electrode was used as an oxygen evolving electrode. Further, the surface-modified iron electrode could sustain current densities as high as 100 mA cm<sup>-2</sup> without any noticeable damage to the coating.

We ascribe the remarkable stability of the surface-modified iron electrode under high anodic currents to the formation of an electrically-conducting mixed hydroxide film by the surface modification process. Such an electrically-conductive layer avoids the damage by dielectric breakdown suffered by insulating films of iron oxide on the unmodified electrodes. Thus, the conversion of the insulating iron oxide surface to other types of electrically-conductive films can also be expected to endow similar stability under anodic conditions. We tested this hypothesis by incorporation of cobalt in the place of nickel, by the same method used here for preparing NSI-200. We then found that the cobalt modification also yielded an iron electrode that was also stable under anodic conditions. Thus, we now have shown a viable approach to stabilizing the iron electrode that is broadly applicable for preventing the degradation and dissolution of iron in alkali under anodic conditions. Such a process for stabilization may be considered akin to the formation of dimensionally stable anodes based on titanium where the surface layer is rendered conducting by forming a conductive solid solution layer of titanium oxide and ruthenium oxide.<sup>55</sup>

While the surface modifications produced on NSI-200 and NSI-400 that were surprisingly stable under anodic conditions, the

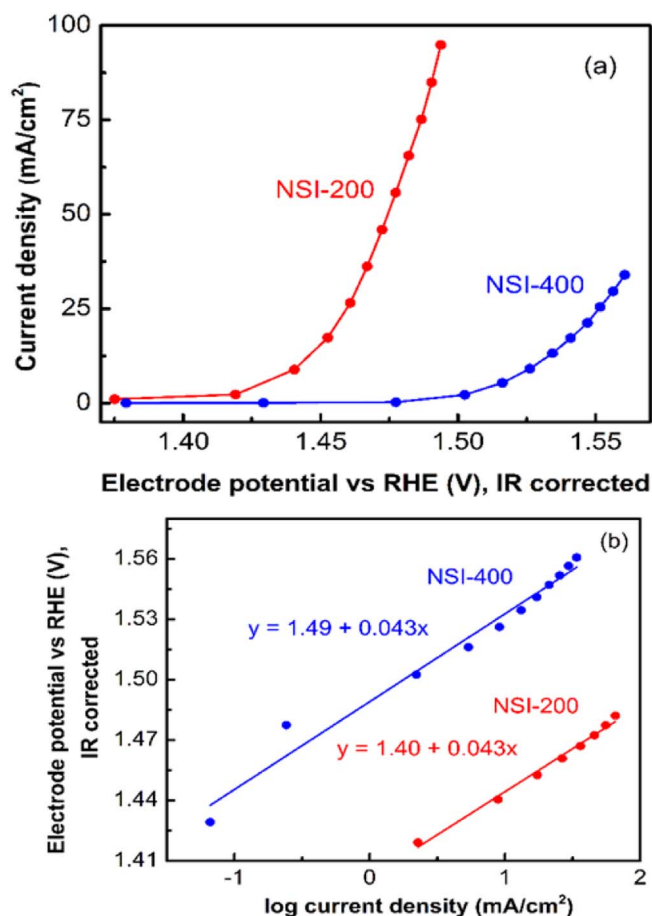


**Figure 8.** (a) Steady State polarization data for oxygen evolution in 5.35 M potassium hydroxide for NSI-200 and NSI-400, (b) Tafel plots after correcting for ohmic losses.

electrocatalytic activity of these modified electrodes for oxygen evolution was even more remarkable (Fig. 8) with significant differences in the performance of NSI-200 and NSI-400. NSI-200 with its particularly high performance and durability emerged as one of the most promising electrocatalysts for oxygen evolution.

The onset potential for oxygen evolution was as low as 1.38 V vs. RHE for NSI-200. This value of onset potential is among the lowest reported thus far for OER on various types of transition metal oxides. The electrode potential for NSI-200 at  $10 \text{ mA cm}^{-2}$  was 1.448 V vs. RHE that corresponded to an overpotential of 218 mV. The roughness factor for NSI-200 was determined to be 6.5 (see supplementary information for calculation). This value of roughness factor is comparable to those reported for other active oxygen evolution catalysts.<sup>16</sup> Therefore, we conclude that NSI-200 has good catalytic activity for oxygen evolution. We have repeatedly observed this high level of performance in three separate electrodes that were prepared similarly. We have ensured that the result is statistically significant and reproducible within 1–2 mV (See Supplementary Information Fig. S4). We note that to reach  $10 \text{ mA cm}^{-2}$  20 wt% Ir/C catalyst requires 380 mV overpotential and 20 wt% Ru/C catalyst requires 390 mV overpotential, respectively.<sup>56</sup>

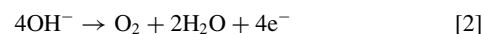
While both NSI-200 and NSI-400 were quite active catalytically for oxygen evolution, NSI-200 was able to sustain 100 times more current than NSI-400 at any particular electrode potential (for example at 1.47 V vs. RHE, Fig. 8b). We observed a Tafel slope of 43 mV/decade for NSI-200 over a wide range of current density (4 to  $100 \text{ mA cm}^{-2}$ ) similar to that observed with the layered nickel and iron hydroxide electrodes.<sup>27,28</sup> A similar Tafel slope of 43 mV/decade was observed

for NSI-400, however, overpotential for NSI-400 at  $10 \text{ mA cm}^{-2}$  was 295 mV (77 mV higher than for NSI-200).

As both NSI-200 and NSI-400 have the same Tafel slope of 43 mV/decade in the range of 5 to  $33 \text{ mA cm}^{-2}$ , we expect that the mechanisms for oxygen evolution are likely to be the same on both surfaces in this region of potentials. The higher current density at any chosen potential observed with NSI-200 may be attributed to the number and type of active sites arising from the higher surface area of NSI-200 compared to NSI-400. Further, we find from XAFS that the NSI-200 sample is characterized by the presence of  $\alpha$ -nickel hydroxide, as compared to the NSI-400 that has largely the nickel ferrite phase. Under anodic conditions,  $\alpha$ -nickel hydroxide will convert to  $\gamma$ -nickel oxyhydroxide that is a more active catalyst than nickel ferrite,  $\text{NiFe}_2\text{O}_4$ .<sup>57</sup>

From the double-layer capacitance measurements (Table I) we conclude that the electrochemically-active surface area of NSI-200 to be as high as 140 times that of NSI-400. The reduced surface area of NSI-400 is consistent with the marked loss of water from the hydroxides that occurs between  $250^\circ\text{C}$  and  $400^\circ\text{C}$  leading to the formation of oxides.<sup>58</sup> Thus, in addition to the differences in the surface composition, the enhanced surface area of NSI-200 could also contribute significantly to the observed activity.

**Reaction mechanism.**—For oxygen evolution in alkali (Eq. 2), the generalized rate equation is given by Eq. 3.



$$\text{Rate} = I/nFA = k(a_{\text{OH}^-})^p \exp(\beta nF(E - E_{\text{rev}})/RT) \quad [3]$$

where  $I$  is the current,  $k$  is the heterogeneous rate constant,  $a_{\text{OH}^-}$  is the activity of hydroxide ions,  $p$  is the order with respect to the hydroxide ion,  $\beta$  is the transfer coefficient,  $F$  is the Faraday constant,  $n$  is the number of electrons transferred in the rate determining step,  $E$  is the electrode potential measured at current  $I$ ,  $E_{\text{rev}}$  is the reversible potential for the oxygen evolution reaction at the specific electrolyte concentration,  $R$  is the gas constant and  $T$  is the absolute temperature.

To gain insight into the reaction mechanism, we determined the order of the reaction with respect to the hydroxide ion from steady-state potentiostatic experiments at different values of concentration of potassium hydroxide solution. We also compared the Tafel slope  $RT/(\beta nF)$  for various mechanisms with the experimental value of the Tafel slope from Fig. 8b. The order of the reaction with respect to hydroxide ions,  $p$  in Eq. 2 is given by,

$$p = [\partial (\log I) / \partial (\log a_{\text{OH}^-})]_{E,T} \quad [4]$$

Specifically, the reaction order was determined from the slope of plot  $\log(\text{current})$  vs  $\log(\text{activity of hydroxide ions})$  at a fixed overpotential and temperature as per Eq. 4. We ensured that the overpotential value was the same at the various values of hydroxide concentration. For such measurements, it was important to correct for the liquid junction potential (see Table S2 in Supplementary information). Also, it was important to use activity values and not simply concentration, as the activity coefficients were significantly different from 1 for the higher concentrations. By this method, we determined the order of reaction with respect to hydroxide ions to be 0.6 (Fig. 9). This value is not far from the values of 0.75 reported for various transition metal oxide surfaces.<sup>59</sup>

The activation energy for oxygen evolution for NSI-200 and NSI-400 were determined from steady-state polarization experiments in 5.35M potassium hydroxide electrolytic-solution by varying the temperature over the range of  $30^\circ\text{C}$  to  $50^\circ\text{C}$  at  $5^\circ\text{C}$  increments. The activation energy,  $\Delta E^\ddagger$ , at various values of electrode potential was calculated from the slope of the Arrhenius-type plots as per Equation 5,

$$\Delta E^\ddagger = -2.303 R [\partial \log I / \partial (1/T)]_E \quad [5]$$

where in,  $R$  is the Universal gas constant,  $I$  is the current,  $T$  is absolute temperature and  $E$  is the electrode potential at current  $I$ . The activation

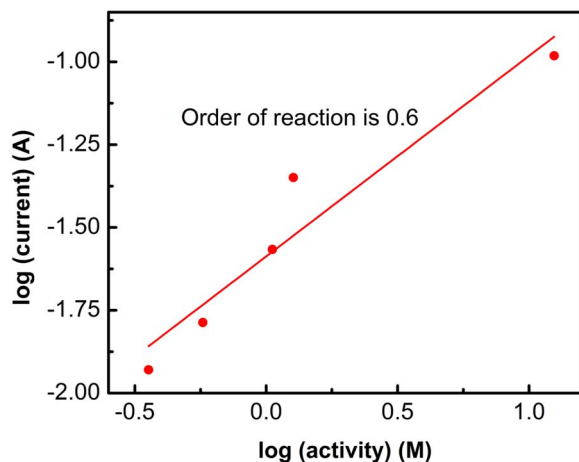


**Figure 9.** Plot of logarithm of current density vs. the logarithm of activity of hydroxide ion at 25°C and 1.6 V vs RHE.

energy for oxygen evolution over the potential range of 1.46 to 1.56 V vs. RHE was in the range of 12 to 18 kcal/mol consistent with the values observed by others for the oxide catalysts<sup>59</sup> (Fig. S5). We can expect the free energy of adsorption to vary with the coverage of hydroxide ions, and hence this variation in activation energy appears to be reasonable to expect.

The values of Tafel slope, activation energy, and the order of reaction with respect to hydroxide ions for NSI-200 were consistent with the O'Grady and Kobussen pathways for the oxygen evolution reaction.<sup>59</sup> The Tafel slope values for the Bockris oxide path was higher than those observed in our studies and consequently, we deemed that this pathway was less likely. The relevant reaction steps for O'Grady and Kobussen pathways are reproduced in Table II.

The observed value of Tafel slope of 43 mV/decade (or approximately,  $2.303 \times 2RT/3F$ ) and the order of reaction with respect to hydroxide of 0.6 is consistent with O'Grady path with the rate-determining step being the electrochemical transformation of surface hydroxides through the change of oxidation state of the transition metal (Step 2). Alternately, the Kobussen pathway could be operating with the rate determining step being an Eley-Rideal type of mechanism leading to surface oxide species (Step 2 of the Kobussen path).

To unequivocally assign one of these mechanisms, we will require knowledge of whether the coverage of the surface by hydroxide is high or low. Since our experiments employ high concentrations of hydroxide, and as the surfaces of NSI-200 and NSI-400 are known to have a strong affinity for hydroxide, a high coverage of hydroxide on the surface can be expected in the potential range of interest. Further, we can expect that the presence of hydroxides and oxides

on the surface of NSI-200 and NSI-400 would allow the formation of superoxy intermediate (M-OOH) via Step 3 leading up to oxygen evolution.<sup>60</sup> Consequently, we conclude that the Kobussen pathway with step 2 as the rate-determining step bears a closer consistency with the electrochemical kinetic data.

**Durability studies.**—For commercial applications in water electrolysis, the electrocatalysts should be durable for thousands of hours. To test the robustness and stability under the conditions of oxygen evolution, we selected NSI-200, our most active catalyst, and held the current at 10 mA cm<sup>-2</sup> in 5.35 M potassium hydroxide solution and monitored the electrode potential for 1000 hours. Such extended durability measurements are not commonly encountered in the catalyst literature, but we realize that this extended durability is an important aspect of the catalyst performance for possible further utilization of these catalyst formulations. The NSI electrode was polarized at 10 mA/cm<sup>2</sup> in a cell consisting of a counter electrode and reference electrode in potassium hydroxide solution, all in the same compartment. A photograph of the cell is included in the supplementary information. The use of a common compartment cell avoided any pH changes at the oxygen evolution electrode. The loss of water of was compensated by the addition of about 5 ml of de-ionized water to the cell. Thus, no change in hydroxide ion concentration occurred during this test. Also reference electrodes were monitored to ensure that there was no drift in their values.

The rate of change in electrode potential over the 1000 hours of testing was estimated by a line fit to be 1.4 μV h<sup>-1</sup>. This extremely low rate of change of potential demonstrated the extraordinary robustness of NSI-200 for OER (Fig. 10). After 700 hours of testing when a slight decrease in overpotential was observed, we noticed that there had been some electrolyte loss from the reference electrode. After refilling of reference electrode, the durability test was resumed and continued, until 1000 hours were completed. Thus, we were able to show that the NSI-200 electrocatalyst formulation was not only electrochemically active but also durable for extended periods. The SEM images confirmed no noticeable change in morphology of the NSI-200 surface even after the 1000 hours of testing, and the high surface area features were retained (Fig. S6).

XPS study for NSI-200 after 1000 hours of oxygen evolution in alkali still showed the presence of Ni<sup>2+</sup>, Fe<sup>3+</sup> and O<sup>2-</sup> on the surface (Fig. 11). Upon comparing the XPS spectra for NSI-200 in Fig. 11 with that of Fig. 7, a peak of very low intensity attributable to iron (0) was still observable. Our observation of iron (0) is consistent with the non-uniform thickness of the coating as revealed by TEM studies (Fig. 6) and the protective nature of the catalytic over-layer. We noted that the XPS data after durability testing showed Fe<sup>3+</sup> and no Fe<sup>2+</sup>, unlike the sample before the test. If the catalytic activity depended on the proportion of Fe<sup>2+</sup>/Fe<sup>3+</sup> sites, it is likely that we would have observed some change in the overpotentials during the durability tests. The absence of this change suggested that the nickel sites are more likely

**Table II.** Mechanistic pathways consistent with the kinetic data for NSI-200 and NSI-400 catalysts.

<b>O'Grady's Path:</b>			
Rate determining step	Tafel slope* at low coverage	Order with respect to OH <sup>-</sup>	
Step 1. M <sup>z</sup> + OH <sup>-</sup> → M <sup>z</sup> OH + e <sup>-</sup>	2RT/F	1	
Step 2. M <sup>z</sup> OH → M <sup>z+1</sup> OH + e <sup>-</sup>	2RT/3F	1	
Step 3. 2M <sup>z+1</sup> OH <sup>-</sup> + 2OH <sup>-</sup> → 2M <sup>z</sup> + 2H <sub>2</sub> O + O <sub>2</sub>	RT/4F	4	
<b>Kobussen's Path:</b>			
Rate determining step	Tafel slope at high coverage	Order with respect to OH <sup>-</sup>	
Step 1. M + OH <sup>-</sup> → MOH + e <sup>-</sup>	-	-	
Step 2. MOH + OH <sup>-</sup> → MO + H <sub>2</sub> O + e <sup>-</sup>	2RT/3F	1	
Step 3. MO + OH <sup>-</sup> → MO <sub>2</sub> H <sup>-</sup>	∞	1	
Step 4. MO <sub>2</sub> H <sup>-</sup> + OH <sup>-</sup> → MO <sub>2</sub> <sup>-</sup> + H <sub>2</sub> O + e <sup>-</sup>	2RT/F	1	
Step 5. MO <sub>2</sub> <sup>-</sup> → M + O <sub>2</sub> + e <sup>-</sup>	∞	0	

\*Note  $2.303 RT/F = 0.059 V$ .

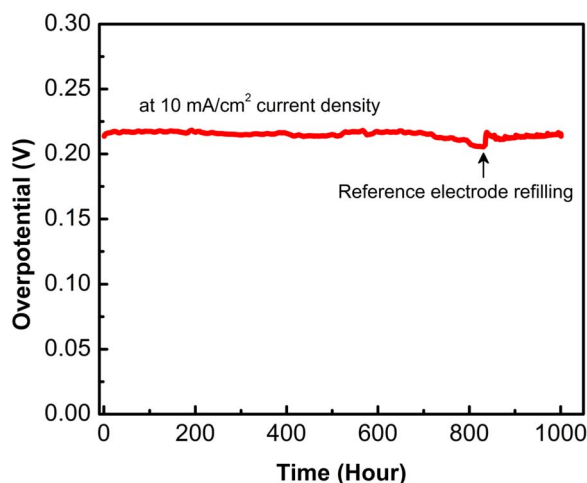


**Figure 10.** Overpotential of NSI-200 electrode at  $10 \text{ mA cm}^{-2}$  in 30% potassium hydroxide at  $25^\circ\text{C}$  monitored over 1000 hours.

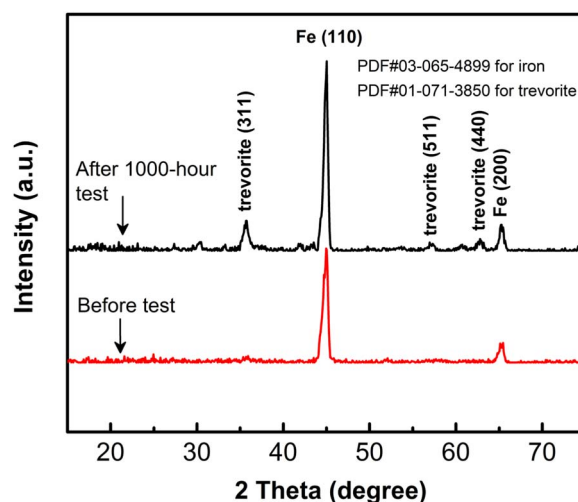


**Figure 12.** Comparison of XRD of NSI-200 before and after 1000-hour anodic polarization test.

to be active site, consistent with the activity of nickel hydroxide coated catalysts reported by others. Also, the nickel continued to remain in the +2 oxidation state after the tests, consistent with the chemical reversibility of the oxidation states of nickel to be expected during oxygen evolution.

XRD studies performed on the samples after the 1000-hour test (Fig. 12) indicated the presence of nanocrystalline nickel ferrite with an estimated crystallite size of 23 nm. XRD results suggested some of the trevorite phase is produced at the end of the durability tests. It is interesting to note that the spinel phase can be produced even at room temperature during electrochemical oxygen evolution. The formation of  $\text{Fe}^{3+}$  noted from XPS is also consistent with some of the surface hydroxides being converted during copious oxygen evolution to the nickel ferrite ( $\text{NiFe}_2\text{O}_4$ ). However, it is possible that the high oxygen concentration at the surface and the ability of the hydroxide groups to diffuse on the surface during electrochemical oxygen evolution could facilitate the transformation to the ferrite at room temperature. Such formation of spinel structures has been known in the anodic oxidation of solutions of cobalt (II) complexes in alkaline media. Spinel crystals prepared electrochemically at room temperature were comparable in crystallinity to the ones produced at elevated temperature.<sup>61</sup> Hence, we can expect the nickel and iron hydroxides that are incompletely

calcined at  $200^\circ\text{C}$  in the NSI-200 to be partially converted to the spinel oxides through oxidation of the alkali soluble solution species. However, it appears that these changes did not have any noticeable impact on the performance of the electrodes over the 1000-hour period. These observations suggested that the  $\alpha$ -nickel hydroxide phase could be the stable active phase supporting the high electrocatalytic activity.

To probe the robustness for even longer duration we have applied  $10 \text{ mA cm}^{-2}$  to one of the NSI-200 electrodes for 1700 hours. Here also we noticed that the rate of change of electrode potential was negligible ( $1 \mu\text{V/h}$ , Fig. S7). This result of extended testing further demonstrated the exceptional durability of the NSI-200 electrodes.

## Conclusions

We have shown that surface-modified iron electrodes combine good electrocatalytic activity with robustness for oxygen evolution. We showed that the surface modification process provided an electrically-conductive layer on the iron electrode that rendered the electrode stable during anodic polarization in alkaline media.

Most importantly, the surface-modified iron electrode exhibited an overpotential of  $0.218 \text{ V}$  at  $10 \text{ mA cm}^{-2}$ . The iron electrode prepared

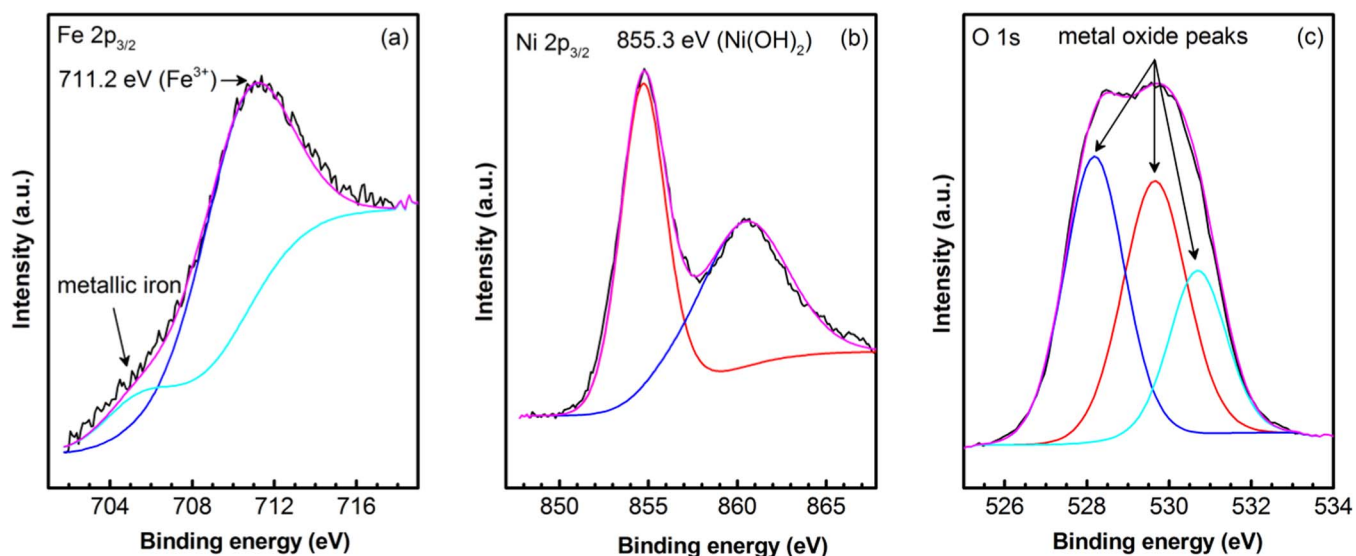


**Figure 11.** XPS measurements on NSI-200 after 1000-hour test.

at 200°C did not show any noticeable change in performance even after 1000 hours of oxygen evolution at a constant current density of 10 mA cm<sup>-2</sup> demonstrating extraordinary robustness of the electrocatalytic coating. The high level of electrochemical activity and stability of the surface-modified iron electrode for oxygen evolution is attributed to the high-surface-area thin layer of  $\alpha$ -nickel hydroxide supported on iron oxides.

The preparation temperature was critical to achieving the high catalytic activity. Raising the preparation temperature from 200°C to 400°C led to dehydration of the hydroxides to the nickel ferrite, loss of surface area and a consequent reduction in electrochemical activity.

The Tafel slope, order of reaction with respect to hydroxide, and the activation energy for the electrochemical reaction were consistent with the Kobussen pathway for oxygen evolution, a pathway particularly applicable for oxide and hydroxide covered surfaces.


By demonstrating the activity and robustness of the surface-modified iron electrode, we have shown the means to an inexpensive electrode alternative to today's nickel-based oxygen-evolution electrodes, and an opportunity to reduce the cost and increase the efficiency of alkaline water electrolysis systems.

### Acknowledgments

The research reported here was supported by the Loker Hydrocarbon Research Institute, and the University of Southern California (USC). We thank Dr. Aswin Manohar and Dr. Chenguang Yang for support with materials and test procedures, and Dr. A. Sundar Rajan for help with the graphics. The TEM samples were prepared at UCLA's Nanolab with the assistance of Noah Bodzin. The TEM imaging and analysis, along with the XPS data, was acquired at USC's Center for Electron Microscopy and Microanalysis (CEMMA). X-ray absorption studies at Sector 20 used resources of the Advanced Photon Source, a U. S. Department of Energy (DOE) Office of Science User Facility operated for the DOE Office of Science by Argonne National Laboratory under Contract No. DE-AC02-06CH11357. We acknowledge Dr. Qing Ma and Denis Keane of DND-CAT for sharing the bent Laue optic.

### ORCID

M. Balasubramanian  <https://orcid.org/0000-0002-3988-3125>

S. R. Narayanan  <https://orcid.org/0000-0002-7259-3728>

### References

1. C. Rerolle and R. Wiert, *Electrochim. Acta*, **41**, 1063 (1996).
2. S. R. Narayan, A. Manohar, and S. Mukerjee, *Electrochem. Soc. Interface*, **24**, 65 (2015).
3. S. Malkhandi, B. Yang, A. K. Manohar, A. Manivannan, G. K. S. Prakash, and S. R. Narayanan, *J. Phys. Chem. Lett.*, **3**, 967 (2012).
4. Z. Pei, H. Li, Y. Huang, Q. Xue, Y. Huang, M. Zhu, Z. Wang, and C. Zhi, *Energy Environ. Sci.*, **10**, 742 (2017).
5. B. Weng, F. Xu, C. Wang, W. Meng, C. R. Grice, and Y. Yan, *Energy Environ. Sci.*, **10**, 121 (2017).
6. A. T. Swesi, J. Masud, and M. Nath, *Energy Environ. Sci.*, **9**, 1771 (2016).
7. *Modern electrochemistry: ionics*, ed. J. O. Bockris, Springer, New York, 1998.
8. F. Song, K. Schenk, and X. Hu, *Energy Environ. Sci.*, **9**, 473 (2016).
9. W. T. Hong, M. Risch, K. A. Stoerzinger, A. Grimaud, J. Suntivich, and Y. Shao-Horn, *Energy Environ. Sci.*, **8**, 1404 (2015).
10. M. W. Kanan and D. G. Nocera, *Science*, **321**, 1072 (2008).
11. H. Dau, C. Limberg, T. Reier, M. Risch, S. Roggan, and P. Strasser, *ChemCatChem*, **2**, 724 (2010).
12. R. K. Hocking, R. Brimblecombe, L. Y. Chang, A. Singh, M. H. Cheah, C. Glover, W. H. Casey, and L. Spiccia, *Nat. Chem.*, **3**, 461 (2011).
13. J. A. Haber, Y. Cai, S. Jung, C. Xiang, S. Mitrovic, J. Jin, A. T. Bell, and J. M. Gregoire, *Energy Environ. Sci.*, **7**, 682 (2014).
14. T. Nakagawa, C. A. Beasley, and R. W. Murray, *J. Phys. Chem. C*, **113**, 12958 (2009).
15. E. Guerrini, H. Chen, and S. Trasatti, *J. Solid State Electrochem.*, **11**, 939 (2007).
16. C. C. McCrory, S. Jung, J. C. Peters, and T. F. Jaramillo, *J. Am. Chem. Soc.*, **135**, 16977 (2013).
17. M. Morimitsu, C. Murakami, K. Kawaguchi, R. Otogawa, and M. Matsunaga, *J. New Mater. Electrochem. Syst.*, **7**, 323 (2004).
18. A. Minguzzi, F. R. F. Fan, A. Vertova, S. Rondinini, and A. Bard, *J. Chem. Sci.*, **3**, 217 (2012).
19. *Atlas of Electrochemical Equilibria in Aqueous Solution*, M. Pourbaix, Pergamon Press: Oxford, 1966, p 373.
20. I. A. Moreno-Hernandez, C. A. MacFarland, C. G. Read, B. S. Brunshwig, K. M. Papadantonakis, and N. Lewis, *Energy Environ. Sci.*, **10**, 2103 (2017).
21. D. E. Hall, *J. Electrochem. Soc.*, **132**, 41C (1985).
22. S. Malkhandi, P. Trinh, A. K. Manohar, A. Manivannan, M. Balasubramanian, G. K. S. Prakash, and S. R. Narayanan, *J. Phys. Chem. C*, **119**, 8004 (2015).
23. K. Jin, A. Chu, J. Park, D. Jeong, S. E. Jerng, U. Sim, H. Y. Jeong, C. W. Lee, Y. S. Park, K. D. Yang, G. K. Pradhan, D. Kim, N. E. Sung, S. H. Kim, and K. T. Nam, *Sci. Rep.*, **5**, 10279 (2015).
24. X. Lu and C. Zhao, *Nat. Commun.*, **6**, 6616 (2015).
25. Y. Zhu, W. Zhou, Z. G. Chen, Y. Chen, C. Su, M. O. Tadé, and Z. Shao, *Angew. Chem. Int. Ed.*, **54**, 3897 (2015).
26. M. S. Burke, M. G. Kast, L. Trotochaud, A. M. Smith, and S. W. Boettcher, *J. Am. Chem. Soc.*, **137**, 3638 (2015).
27. M. Gong, Y. Li, H. Wang, Y. Liang, J. Z. Wu, J. Zhou, J. Wang, T. Regier, F. Wei, and H. Dai, *J. Am. Chem. Soc.*, **135**, 8452 (2013).
28. F. Song and X. Hu, *Nat. Commun.*, **5**, 4477 (2014).
29. J. Suntivich, K. J. May, H. A. Gasteiger, J. B. Goodenough, and Y. Shao-Horn, *Science*, **334**, 1383 (2011).
30. A. Grimaud, K. J. May, C. E. Carlton, Y. L. Lee, M. Risch, W. T. Hong, J. Zhou, and Y. Shao-Horn, *Nat. Commun.*, **4**, 2439 (2013).
31. W. Zhou and J. Sunarso, *J. Phys. Chem. Lett.*, **4**, 2982 (2013).
32. T. W. Kim, M. A. Woo, M. Regis, and K. S. Choi, *J. Phys. Chem. Lett.*, **5**, 2370 (2014).
33. M. K. Bates, Q. Jia, H. Doan, W. Liang, and S. Mukerjee, *ACS Catal.*, **6**, 155 (2015).
34. M. W. Louie and A. T. Bell, *J. Am. Chem. Soc.*, **135**, 12329 (2013).
35. S. Klaus, M. W. Louie, L. Trotochaud, and A. T. Bell, *J. Phys. Chem. C*, **119**, 18303 (2015).
36. J. Zhang, Z. Zhao, Z. Xia, and L. Dai, *Nat. Nanotechnol.*, **10**, 444 (2015).
37. D. Friebe, M. W. Louie, M. Bajdich, K. E. Sanwald, Y. Cai, A. M. Wise, M. J. Cheng, D. Sokaras, T. C. Weng, R. Alonso-Mori, and R. C. Davis, *J. Am. Chem. Soc.*, **137**, 1305 (2015).
38. M. Gong and A. H. Dai, *Nano Res.*, **8**, 23 (2015).
39. H. S. Ahn and A. J. Bard, *J. Am. Chem. Soc.*, **138**, 313 (2016).
40. R. Fayad, J. Dhainy, H. Ghandour, and L. Halaoui, *Catal. Sci. Technol.*, **7**, 3876 (2017).
41. M. Görlin, P. Chernev, J. F. de Araújo, T. Reier, S. Dresch, B. Paul, R. Krähnert, H. Dau, and P. Strasser, *J. Am. Chem. Soc.*, **138**, 5603 (2016).
42. M. Hayes and A. T. Kuhn, *J. Appl. Electrochem.*, **8**, 327 (1978).
43. R. D. Smith, M. S. Prévot, R. D. Fagan, S. Trudel, and C. P. Berlinguette, *J. Am. Chem. Soc.*, **135**, 11580 (2013).
44. B. Ravel and M. A. Newville, *J. Synchrotron Radiat.*, **12**, 537 (2005).
45. H. S. Harned, *J. Am. Chem. Soc.*, **47**, 689 (1925).
46. G. J. Brug, A. L. G. van den Eeden, M. Sluyters-Rehbach, and J. H. Sluyters, *J. Electroanal. Chem. Interfacial Electrochem.*, **176**, 275 (1984).
47. A. M. Gadalla and T. W. Livingston, *Thermochim. Acta*, **145**, 1 (1989).
48. A. N. Mansour and C. A. Melendres, *J. Phys. Chem. A*, **102**, 65 (1998).
49. M. Balasubramanian, C. A. Melendres, and A. N. Mansour, *J. Electrochem. Soc.*, **146**, 607 (1999).
50. D. Carta, M. F. Casula, A. Falqui, D. Loche, G. Mountjoy, C. Sangregorio, and A. Corrias, *J. Phys. Chem. C*, **113**, 8606 (2009).
51. C. N. Chinnasamy, A. Narayanasamy, N. Ponpandian, K. Chattopadhyay, K. Shinoda, B. Jeyadevan, K. Tohji, K. Nakatsuka, T. Furubayashi, and I. Nakatani, *Phys. Rev. B*, **63**, 184108 (2001).
52. L. Trotochaud, S. L. Young, J. K. Ranney, and S. W. Boettcher, *J. Am. Chem. Soc.*, **136**, 6744 (2014).
53. *Handbook of X-ray photoelectron spectroscopy*, ed. G. E. Muilenberg, Perkin-Elmer Corp., 1979.
54. A. P. Grosvenor, M. C. Biesinger, R. S. Smart, and N. S. McIntyre, *Surf. Sci.*, **600**, 1771 (2006).
55. S. Trasatti, *Electrochim. Acta*, **45**, 2377 (2000).
56. Y. Gorlin and T. F. Jaramillo, *J. Am. Chem. Soc.*, **132**, 13612 (2010).
57. P. Oliva, J. Leonardi, J. F. Laurent, C. Delmas, J. J. Braconnier, M. Figlarz, F. Fievet, and A. De Guibert, *J. Power Sources*, **8**, 229 (1982).
58. D. H. Chen and X. R. He, *Mater. Res. Bull.*, **36**, 1369 (2001).
59. J. O. Bockris and T. Otagawa, *J. Phys. Chem.*, **87**, 2960 (1983).
60. J. Rossmeisl, A. Logadottir, and J. K. Nørskov, *Chem. Phys.*, **319**, 178 (2005).
61. K. Nakaoka, M. Nakayama, and K. Ogura, *J. Electrochem. Soc.*, **149**, C159 (2002).